SCIENTIFIC REPORTS
nature research

Check for updates

OPEN

Photoelectrochemical and crystalline properties of a GaN photoelectrode loaded with α-Fe_2O_3 as cocatalyst

Martin Velazquez-Rizo, Daisuke Iida & Kazuhiro Ohkawa✉

Nitrides are of particular interest in energy applications given their suitability to photocatalytically generate H_2 from aqueous solutions. However, one of the drawbacks of nitrides is the decomposition they suffer when used in photoelectrochemical cells. Here, we report the improvement of the catalytic performance and chemical stability of a GaN electrode when it is decorated with Fe_2O_3 particles compared with an undecorated electrode. Our results show a higher reaction rate in the Fe_2O_3/GaN electrode, and that photocorrosion marks take more than 20 times longer to appear on it. We also characterized the crystalline properties of the Fe_2O_3 particles with transmission electron microscopy. The results show that the Fe_2O_3 particles keep an epitaxial relationship with GaN that follows the $Fe_2O_3\{0003\}||GaN\{0001\}$ and $Fe_2O_3[11\bar{2}0]||GaN[1\bar{1}00]$ symmetry constraints. We also characterized an Fe_2O_3 (thin film)/GaN electrode, however it did not present any catalytic improvement compared with a bare GaN electrode. The epitaxial relationship found between the Fe_2O_3 thin film and GaN exhibited the $Fe_2O_3\{11\bar{2}0\}||GaN\{0002\}$ and $Fe_2O_3[3\bar{3}00]||GaN[11\bar{2}0]$ symmetry constraints.

The increasing energy demand of humankind and the negative environmental impact of the consumption of fossil fuels are driving the development of alternative energy sources. One of the candidates to substitute fossil fuels is H_2, which can generate energy through its direct combustion or in fuel cells without creating pollution. However, the non-pollutant attributes of H_2 have been overshadowed by the lack of an environmentally friendly method for its manufacture.

One alternative to sustainably generate H_2 is the photocatalytic water splitting using semiconductors[1]. Nitrides have received considerable attention in this field because, as a result of their band gap tunability[2–8], they can absorb most of the energy of the solar spectrum. After the first demonstration of photoelectrochemical (PEC) H_2 generation using GaN thin films as photoelectrodes[9], and their subsequent improvement to perform chemical reactions without any external electrical bias[10], the discovery of the NiO cocatalyst technology[11] greatly boosted the expectations of nitride-based photocatalysts. NiO cocatalyst improved not only the Energy Conversion Efficiency (ECE) of nitride photoelectrodes, but also their lifetime, which has been demonstrated to be at least 500 h[12]. It has also been confirmed that NiO/nitride photoelectrodes can be used to generate more complex byproducts than H_2, such as formic acid and methane from CO_2 in artificial photosynthesis reactions[13–16].

The improvement of the catalytic activity of GaN photoanodes by using metals or metal oxides as cocatalysts can be attributed to the introduction of active sites by the metal or oxygen atoms. For example, in water splitting on metal oxides, the Oxygen Evolution Reaction (OER) mechanism has been described conventionally as a four proton–electron transfer reaction in the metal-sites[17,18]. The OER activity of this mechanism is controlled by tuning the oxygen affinity of the adsorbed reaction intermediates. There is also evidence of another catalytic route where the lattice-oxygen participates in the reaction via the reversible formation of a superficial oxygen vacancy[19,20]. This mechanism shows that not only the electronic properties of the metal oxide surface are important but also its bulk electronic structure. The ECE of nitride-based photocatalysts can be improved if the role of their cocatalysts is understood. Finding new cocatalysts and analyzing the features they share with known cocatalyst materials, such as NiO, Ag[21], Pt[22], $Rh_{2-y}Cr_yO_3$[23] and CoO_x[24,25] is a crucial step towards the comprehension

Computer, Electrical and Mathematical Sciences and Engineering (CEMSE) Division, King Abdullah University of Science and Technology (KAUST), Thuwal 23955-6900, Saudi Arabia. ✉email: kazuhiro.ohkawa@kaust.edu.sa

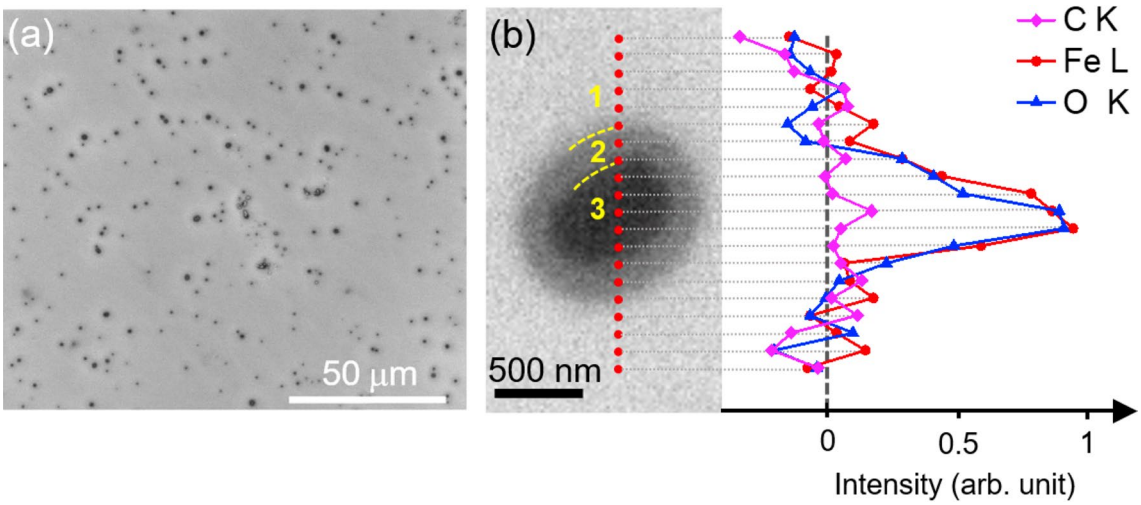

Figure 1. (**a**) SEM micrograph of the Fe_2O_3/GaN electrode surface. The dark spots are the Fe_2O_3 particles deposited as cocatalysts. The energy dispersive X-ray spectroscopy analysis along the red dotted line in (**b**) confirmed the presence of Fe and O only in the region 3.

of their role in photocatalytic reactions. Moreover, it is preferable to find cocatalysts made of non-noble metals because of their availability and cost.

Hematite (α-Fe_2O_3, α is omitted henceforth) is a transition metal oxide that has been widely used and studied as photocatalyst and cocatalyst in water splitting and other chemical reactions, either alone or in combination with other materials[26–32]. However, there is little available information about its suitability to improve the photocatalytic properties of nitrides. In this work, we report the improvement of the catalytic activity in a GaN electrode decorated with Fe_2O_3 particles compared with a bare GaN electrode. Despite such improvement may be attributed to the introduction of active sites by Fe or O atoms in the Fe_2O_3, we propose a mechanism more consistent with our observations. The higher catalytic activity when the Fe_2O_3 is deposited as particles instead of as a thin film and the local formation of n^--n junctions suggest an enhancement due to the easier charge transport directly from GaN to the electrolyte. In addition, we present the characterization of the surface of the photoelectrode with Scanning Electron Microscopy (SEM) and the study of the crystalline properties of the cocatalyst with different Transmission Electron Microscopy (TEM) analytical techniques, including Electron Energy-Loss Spectroscopy (EELS).

Results and discussion

We measured the size of the iron oxide particles using SEM observations. The particles had an average size of 1 μm. The optimal GaN surface coverage by the iron oxide particles was 1.3%, which agrees with previous reports of optimal GaN coverage by NiO cocatalyst[12]. Figure 1a shows the iron oxide particles deposited on GaN as dark spots. A magnification of one of those spots is shown in Fig. 1b, where three different-contrast regions are identified by numbers from 1 to 3. The Energy Dispersive X-ray spectroscopy (EDX) profiles of C, Fe and O along the red dotted line of Fig. 1b confirmed the presence of Fe and O only in region 3, and we discarded the non-uniform presence of carbon in the whole mapped region because the EDX carbon profile did not present significant variations. Therefore, the observation of the transition region (region 2) surrounding the Fe_2O_3 particle was not caused by different material compositions, though it can be related to a local change in the carrier concentration of GaN[33,34].

The local variation in carrier concentration around the Fe_2O_3 particles can be originated either from the solid phase diffusion of Fe atoms into GaN during the annealing process after the cocatalyst deposition, or by the formation of a junction between GaN and Fe_2O_3. Although it has been shown that Fe atoms can diffuse into GaN as far as 1 μm if it is annealed at 1,050 °C[35], the low temperature of our annealing process (500 °C) and the exponential dependence of the diffusion coefficient on temperature suggest that the doping effect is not considerable. Besides, Fe atoms in GaN act as acceptor-like point defects[36], decreasing the n-type carrier concentration of GaN. Thus, a GaN region containing Fe diffused atoms would generate a brighter contrast in SEM than the unintentionally doped (uid)-GaN, rather than the darker contrast observed. Because Fe_2O_3 is typically an n-type semiconductor[37], we believe that the formation of a n^--GaN/n-Fe_2O_3 junction is the cause of the transition region observed around the Fe_2O_3 particle. This heterojunction would induce a negative charge accumulation in the GaN region surrounding the Fe_2O_3 particle that should present a darker contrast in SEM than uid-GaN, which agrees with our observations.

The identification of the iron oxide stoichiometry and phase were done by the study of the chemical and crystalline properties of the iron oxide particles. Figure 2a shows the scanning TEM micrograph of the interface between GaN and Fe_2O_3. Figure 2b–e show the EELS elemental mappings of Ga, N, Fe and O, respectively, of the area enclosed by the red rectangle in Fig. 2a. In those mappings, GaN and iron oxide regions are clearly separated,

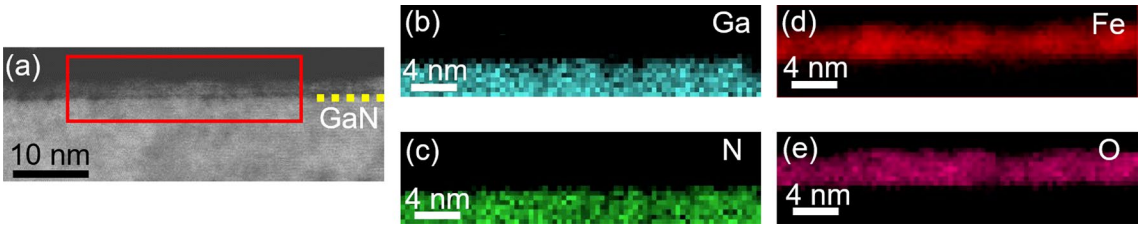

Figure 2. (**a**) Cross-sectional scanning TEM micrograph of the Fe_2O_3/GaN electrode. (**b**)–(**e**) EELS elemental mapping of Ga, N, Fe and O in the zone enclosed by the red rectangle marked in (**a**).

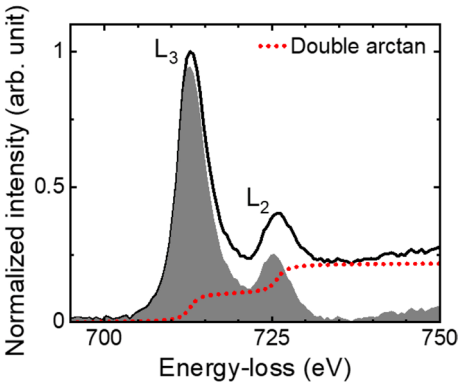

Figure 3. Electron energy-loss near-edge structure of Fe $L_{2,3}$-edge, obtained from the iron oxide region analysed by EELS. The gray region represents the difference between the energy-loss spectrum (solid line) and the double arctan continuum model (broken red line).

and there was no observable diffusion of O and Fe into the GaN region within the detection limits of the EELS analysis. The thickness of the iron oxide in the region observed was about 3 nm.

The presence of the α phase of Fe_2O_3 can be confirmed by the ferric iron concentration ($Fe^{3+}/\Sigma Fe$) derived from the Fe electron Energy-Loss Near-Edge Structure (ELNES) presented in Fig. 3. The ELNES data was obtained from the iron oxide region mapped by EELS in Fig. 2. The maximum of the L_3 and L_2 peaks were found at 712.8 and 725.8 eV, respectively. The L_3/L_2 white-line intensity ratio and $Fe^{3+}/\Sigma Fe$ were calculated after extracting the background with a double arctan function as the continuum model and using integration windows (2 eV width) centered on the peaks[38]. The L_3/L_2 white-line intensity ratio found in our analysis was 3.9, corresponding to a $Fe^{3+}/\Sigma Fe$ of 44% based on the calibration done in ref.[38], which is lower than the expected value of 100% in α-Fe_2O_3. Nonetheless, the iron in the cocatalyst particles was susceptible to the interaction with the carbon deposited directly on the photoelectrode surface by the electron beam during the lamella preparation. Therefore, given the thickness of the Fe_2O_3 particle, we believe that there was a substantial reduction of Fe^{3+} atoms to Fe^{2+} in the lamella preparation process.

Despite the $Fe^{3+}/\Sigma Fe$ found was low to confirm that the iron oxide was α-Fe_2O_3, the lattice spacings observed through High-Resolution TEM (HRTEM) correspond only to α-Fe_2O_3 in the $[1\bar{1}00]$. zone axis and not to any other phase of Fe_2O_3 nor mixed oxide of Fe^{2+} and Fe^{3+}. The HRTEM micrograph displayed in Fig. 4a shows the cross-sectional view of the Fe_2O_3/GaN interface. Based on the lattice spacings found and the lattice constants of α-Fe_2O_3 ($a = 5.038$ Å and $c = 13.772$ Å)[39] and wurtzite GaN ($a = 3.189$ Å and $c = 5.185$ Å)[5], some crystallographic orientations were marked in the Fe_2O_3 and GaN regions. The in-plane lattice mismatch between Fe_2O_3 and GaN is 58%. However, due to the orientation relationship between Fe_2O_3 and GaN, the interplanar spacing mismatch is only 9%.

Figure 4b shows a close-up of the red rectangle marked in Fig. 4a, with the GaN and Fe_2O_3 crystal projections superposed (oriented as indicated in Fig. 4a) in one of their possible configurations. The observation of high distortion of the lattice grids of GaN and Fe_2O_3 near their interface is localized in a transition layer with a thickness of only 8 Å, highlighted in yellow in Fig. 4a,b. The size of the transition layer and the evidence of no diffusion of iron into the GaN region indicates an abrupt Fe_2O_3/GaN interface. Even though we did not observe any constraint in the lattice size of Fe_2O_3 imposed by the influence of GaN, we recognized that the recrystallization orientation of Fe_2O_3 kept a particular epitaxial relationship, which followed the $Fe_2O_3\{0003\}||GaN\{0001\}$ and $Fe_2O_3[11\bar{2}0]||GaN[1\bar{1}00]$ symmetry constraints, equivalent to those previously reported[40]. Such epitaxial relationship is potentially generated due to the similar hexagonal symmetry of the planes perpendicular to the *c*-axis formed by oxygen in Fe_2O_3 and Ga or N in GaN.

Regarding the PEC characterization of the Fe_2O_3/GaN and bare GaN electrodes, the study of the oxidation half-reaction by Cyclic Voltammetry (CV) allowed us to compare qualitatively their performance as photoanodes. Figure 5 contains the first and tenth cycles of the CV measurements of such electrodes. The dark currents were

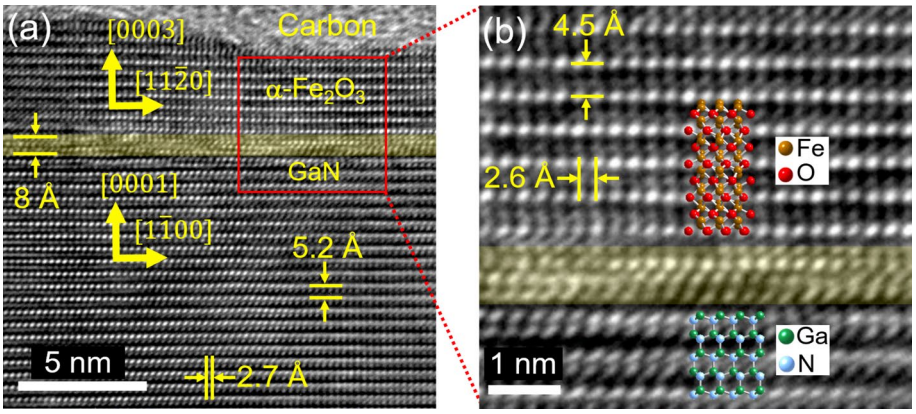

Figure 4. (**a**) HRTEM of the Fe_2O_3/GaN interface. (**b**) Magnification of the red rectangle highlighted in (**a**). Some crystallographic directions are displayed based on the lattice spacings of GaN and α-Fe_2O_3. In (**b**), the crystal projections of Fe_2O_3 and GaN oriented as indicated in (**a**) are overlapped in the lattice fringes in one of their possible configurations. The translucent yellow stripes in (**a**) and (**b**) show the zone of high distortion of lattice fringes at the Fe_2O_3/GaN interface.

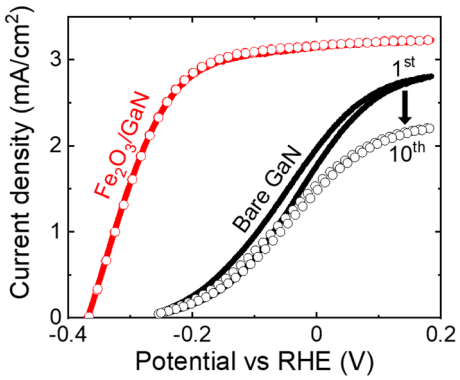

Figure 5. Cyclic voltammogram traces of the Fe_2O_3/GaN and bare GaN electrodes at a scanning speed of 20 mV/s. The solid lines represent the current density during the 1st cycle of the measurements and the scattered data during the 10th cycle.

negligible and are not shown. The election of measuring only 10 cycles in the CV characterization was done based on the quick degradation of the photocurrent of the bare GaN electrode, though the traces of the Fe_2O_3/GaN electrode were almost identical. The behavior of both electrodes in this characterization was similar but with a potential shifting: they presented a steady current density increase until they reach a plateau. The plateau level of the bare GaN electrode is barely reached within the voltage interval used in the measurements, but it is clearly reached in the Fe_2O_3/GaN electrode because of its large negative potential shifting. For example, at a current density of 1 mA/cm^2, the potential of the Fe_2O_3/GaN electrode was about 0.2 V lower than the potential of the bare GaN electrode.

In general, the flat-band potential follows the trend of the onset voltage[41]. Thus, the observable shifting in the CV behavior of both electrodes can be attributed to the different potential at their surfaces, caused by the presence or absence of the cocatalyst. The negative potential shift and the higher photocurrent in the plateau region observed in the voltammogram of the Fe_2O_3/GaN electrode are evidence of its higher reaction rate compared with the bare GaN electrode[26].

The results of the two-electrode PEC characterization to study the zero-bias H_2 generation of both photoelectrodes are shown in Fig. 6. The H_2 and O_2 generated by the platinum cathode and the Fe_2O_3/GaN anode, respectively, are presented in Fig. 6a, where it is shown that the H_2 generation rate remained stable in each characterization, with an average over the five rounds of characterization of 11.5 nmol/cm^2 s. As a comparison, Fig. 6b,c show the H_2 generation and current density, respectively, of the PEC cell during the fifth round of characterization (40–50 h) of the Fe_2O_3/GaN anode, and the first and unique round of characterization of the bare GaN electrode (0–10 h). To compare the performance of both electrodes in this characterization, we used as a figure of merit the ECE, defined by:

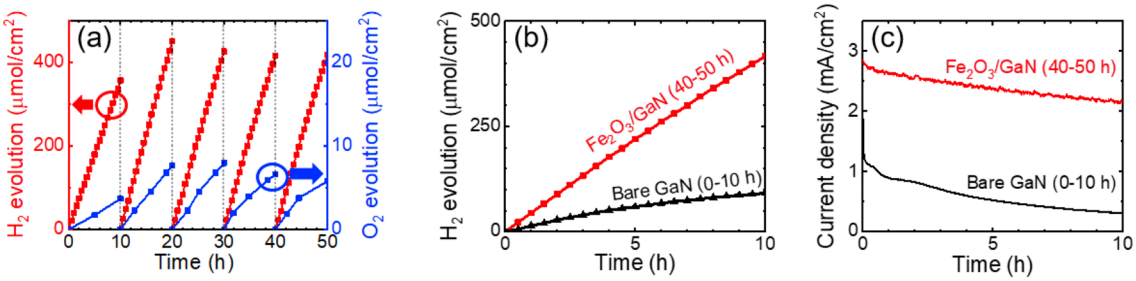

Figure 6. (**a**) H_2 and O_2 evolution on the platinum cathode and Fe_2O_3/GaN anode, respectively, during 50 h of zero-bias PEC characterization. Comparison of the (**b**) H_2 evolution at the cathode and (**c**) photocurrent of the PEC cell during the fifth round of characterization (40–50 h) of the Fe_2O_3/GaN anode, and the unique characterization of the bare GaN anode (0–10 h).

$$\eta_H = \frac{n\Delta G}{P} \tag{1}$$

where n is the H_2 generation rate (mol/cm^2 s), ΔG is the Gibbs free energy of H_2 combustion with O_2 (237.1 kJ/mol) and P is the optical power density irradiated (100 mW/cm^2). The ECE of the of the Fe_2O_3/GaN electrode in its five rounds of characterization were 2.3%, 3.0%, 2.8%, 2.7% and 2.7%. The bare GaN electrode reached an ECE of only 0.6%. Based on the comparison of the light source used in our PEC experiments with the standard AM 1.5G spectrum, we can estimate that our calculated ECE is about 11 times higher than the standard solar-to-hydrogen ECE. The faradaic efficiencies of the H_2 evolution in the five rounds of the PEC characterization of the Fe_2O_3/GaN electrode were 85%, 100%, 93%, 84% and 90%. Although the faradaic efficiencies related to the H_2 generation agree with the values expected in water splitting, the O_2 generation at the Fe_2O_3/GaN electrode was lower than the one expected in this reaction. The maximum H_2:O_2 ratio obtained was 2:0.03, indicating an oxygen generation of only 3% of the stoichiometric amount expected in water splitting. This result suggests that the photogenerated holes were not only involved in the O_2 generation reaction, but also in other side reactions. For instance, Ito et al. (1984)[42] demonstrated that the presence of epoxy resin in a PEC cell generate liquid organic byproducts when it is irradiated with UV light. Given that the illumination source of our experiments is mostly UV light, the decomposition of epoxy resin and the interaction of its organic byproducts and the photogenerated holes in the GaN anode can occur. In fact, the generation of bubbles at the anodes was poor, which indicates that the photoelectrodes were driving reactions whose byproducts were not in gas phase but in liquid phase. Those reactions may have a lower potential than the necessary for water splitting, therefore, the ECE parameter calculated as a figure of merit by Eq. (1) would be overestimated compared with the real ECE of the electrodes.

One of the benefits of incorporating a cocatalyst in the GaN electrode surface is the prevention or retardation of the GaN photocorrosion. While the bare GaN electrode exhibited macroscopic signals of photocorrosion[43,44] within the first 2 h of PEC characterization (loss of the mirror-like finish of the GaN surface), the Fe_2O_3/GaN electrode exhibited these photocorrosion marks after 43 h and only near the metallic contact of the electrode. Thus, the appearance of photocorrosion marks was retarded more than 20 times. Figure 7a shows a picture of the surface of the Fe_2O_3/GaN electrode after 50 h of two-electrode PEC characterization, where the metallic contact region covered with epoxy resin is observable at the bottom of the picture. The Atomic Force Microscope (AFM) topographic profile in Fig. 7b of the electrode a few millimeters away from the metallic contact (blue square in Fig. 7a) shows that the electrode preserves its smooth flat surface in that region. In contrast, the topographic profile presented in Fig. 7c of the region close to the metallic contact (red square in Fig. 7a) shows an etching depth of at least 140 nm. As a comparison, the topographic profile of the bare GaN electrode after the two-electrode PEC characterization is shown in Fig. 7d. This electrode exhibited etched regions with a depth of more than 300 nm; however, the etching was present over the whole electrode surface and only after 10 h of characterization. The localized surface damage of the Fe_2O_3/GaN can be explained by the short distance between its metallic contact and the etched regions. The electron extraction is more difficult in the region far from the contact than in the region close to it due to the higher electrical resistance that the n-GaN layer represents. Therefore, the recombination of the electron–hole pairs generated during the photoabsorption process will be higher in the region far from the contact. The higher population of free holes near the contact would be able to drive the oxidation of species more easily, including GaN, which would be reflected in a faster photocorrosion of the electrode in that region[45].

The H_2 generation of our PEC cell using the Fe_2O_3/GaN and bare GaN electrodes is consistent with their CV characterizations. The best performance observed in both PEC characterizations corresponds to the Fe_2O_3/GaN electrode. As mentioned above, the bare GaN electrode suffered a quick degradation in their photocurrent, observable in the difference of the photocurrent trace in as few as ten cycles of its CV characterization, and also observable in the quick decay of its photocurrent in the first hour of its two-electrode characterization, presented in Fig. 6c. Despite the Fe_2O_3/GaN electrode has demonstrated an improvement in the photocatalytic reaction and photocorrosion retardation, its performance is slightly inferior when compared with a NiO/GaN electrode. Under the same experimental conditions, a NiO/GaN electrode reached a maximum ECE of 3.3% (see Supplementary Figure S1), and after 50 h of PEC characterization it did not show any marks of photocorrosion.

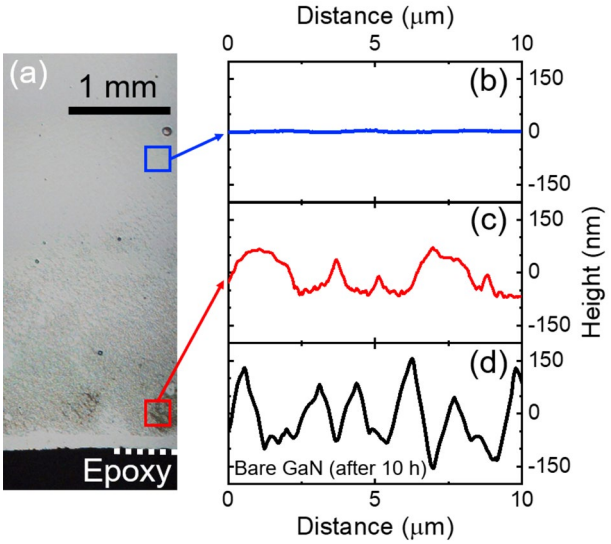

Figure 7. (**a**) Optical microscope image of the surface of the Fe_2O_3/GaN electrode after 50 h of PEC characterization. At the bottom, the epoxy resin covering the metallic contact of the electrode is observable. The AFM topographic profiles of the Fe_2O_3/GaN electrode around the blue and red regions marked in (**a**) are presented in (**b**) and (**c**), respectively. The topographic profile of the bare GaN photoelectrode surface after 10 h of PEC characterization is presented in (**d**).

The O_2 generated by this electrode was 11% of the amount expected in water splitting, and while it is still low, it is certainly higher than the 3% generated by the Fe_2O_3/GaN electrode.

The improvement of the catalytic activity of the Fe_2O_3/GaN electrode due to the presence of the iron oxide particles might be a consequence of the introduction of active sites either by the Fe or O atoms. However, if this is the case, an Fe_2O_3 thin film would improve further the catalytic activity of GaN due to a larger introduction of active sites. To verify this idea, we prepared and characterized an Fe_2O_3 (thin film)/GaN electrode. The thickness of the Fe_2O_3 layer was 2.5 nm (see Supplementary Figure S2), comparable with the thickness of the iron oxide particles (3 nm) and thus presenting a similar electrical resistance between GaN and the electrolyte. The Fe_2O_3 layer also exhibited and epitaxial relationship with GaN, but with the $Fe_2O_3\{11\bar{2}0\}||GaN\{0002\}$ and $Fe_2O_3[3\bar{3}00]||GaN[11\bar{2}0]$ symmetry constraints (see Supplementary Figure S3), different from the constraints found in the Fe_2O_3 particles. The ECE of this electrode reached a value of only 0.6% (see Supplementary Figure S4), which is the same value reached by the bare GaN electrode, but after 10 h of PEC characterization it did not show any marks of photocorrosion. The inferior catalytic performance of a GaN electrode when using an Fe_2O_3 thin film as cocatalyst instead of Fe_2O_3 particles can be caused by the different crystallographic planes at the surface of the Fe_2O_3 given the different epitaxial relations found. Nonetheless, the catalytic properties of the $Fe_2O_3(11\bar{2}0)$ and $Fe_2O_3(0001)$ orientations seem to be similar. For example, theoretical calculations have shown that the OER overpotential between the $Fe_2O_3(11\bar{2}0)$ and $Fe_2O_3(0001)$ orientations is not significant[46]. Thus, the performance of the Fe_2O_3 (thin film)/GaN electrode is inferior because the active sites are not introduced by the iron oxide. Instead, we believe that the improvement of the catalytic activity might be a consequence of the formation of accumulation layers in GaN (region 2 in Fig. 1b) due to the n^--GaN/n-Fe_2O_3 junction. The extraction of holes in the junction between these accumulation layer regions and the electrolyte would be improved by the higher band bending of GaN at the surface of these regions compared with the original uid-GaN (as a result of their difference in carrier concentration). The sparsity of such regions also brings the advantage of preserving the photoabsorption properties of the bulk GaN.

Methods

Photoelectrode structure. The GaN structure of the photoelectrodes was grown by metalorganic vapor phase epitaxy on a *c*-plane conical-patterned sapphire substrate (PSS) with a pattern pitch, diameter, and height of 3.0, 2.6 and 1.6 μm, respectively. The homostructure consisted of (top to bottom) uid-GaN (100 nm)/n-GaN (Si-doped, $n = 3 \times 10^{18}$ cm^{-3}, 3 μm)/uid-GaN (2 μm). A schematic of the cross-sectional view of the Fe_2O_3/GaN electrode is presented in Fig. 8. The PSS improves the crystalline quality of the electrode structure because when GaN is grown on it, its dislocations tend to merge, reducing the overall number of crystal defects. Given that the initial GaN layer has the possibility of trapping carriers via defects, it needs to be non-conductive. Therefore, the underlying GaN was chosen to be unintentionally doped so it has a low electrical conductivity. The objective of the top uid-GaN layer was to extend the depletion layer to a thickness comparable to the light penetration depth of GaN. This increase of the depletion layer optimize the charge separation after the photoabsorption process[47]. While the holes are directed to the surface of the electrode to perform oxidation reactions, the electrons should be transported out of the GaN structure to the counterelectrode, where the reduction reactions take place. How-

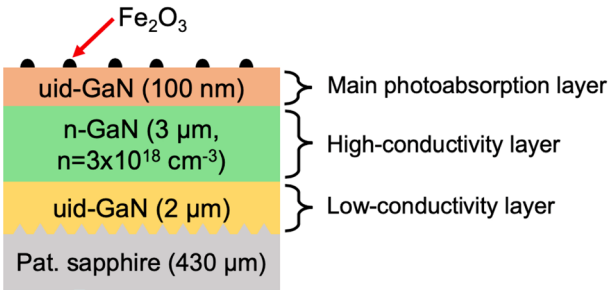

Figure 8. Schematic of the cross-sectional view of the Fe_2O_3/GaN electrode.

ever, uid-GaN has a high electrical resistance, thus, to facilitate the electron extraction of the GaN photoelectrode, we introduced the underneath n-GaN layer, which provides a low-resistance electrical path.

Cocatalyst deposition. The deposition of the Fe_2O_3 and NiO cocatalysts was done by spin coating a diluted Metalorganic Decomposition Solution (MOD). The MOD solution contained 3 wt% of either Fe_2O_3 or NiO. The MOD solution for the Fe_2O_3 particles deposition was diluted in a Fe_2O_3 MOD:butyl acetate:H_2O ratio (by volume) of 2:100:30, and for the Fe_2O_3 thin film it was diluted in a Fe_2O_3 MOD:butyl acetate ratio of 1:20. In the case of the NiO cocatalyst, the NiO MOD was diluted in a NiO MOD:butyl acetate:H_2O ratio of 11:1,000:300. All the substrates were spun at a speed of 2,000 rpm for 30 s after the cocatalyst solution was deposited on each one and, ultimately, annealed at 500 °C for 30 min in air.

Photoelectrode preparation. The substrates were prepared as photoelectrodes by soldering a copper wire to their surface using indium to create an ohmic contact between the wire and GaN. The copper and indium on the surface of the photoelectrode were electrically isolated by covering them with epoxy resin. In this manner, once the photoelectrodes were immersed in the aqueous solution (1 M NaOH) for the PEC characterizations, no metal was in contact with the electrolyte.

Electron microscopy analyses. The surface of the Fe_2O_3/GaN electrode was characterized by SEM observations complemented with EDX using a FEI Magellan microscope operating at 3 and 5 kV. For the TEM analysis, a cross-sectional TEM lamella was prepared by focused ion beam (Ga) milling using a FEI Helios DualBeam (FIB/SEM) microscope. The surface of the lamella region was protected with electron-beam-deposited carbon and platinum, followed by ion-beam-deposited platinum. HRTEM observations and EELS analyses were done in a FEI Titan microscope operating at 300 kV. The EELS data was obtained in the scanning TEM mode using the dual-EELS technique to simultaneously acquire the core-loss and low-loss spectra. The energy dispersion was 0.5 V per channel and the energy drift was corrected by correlating the zero-loss peak positions obtained in the low-loss spectra with the core-loss spectra.

PEC characterizations. The PEC characterizations of the photoelectrodes were done in two parts: linear sweeping CV in a three-electrode setup (sweeping speed of 20 mV/s) and measurements of the zero-bias H_2 generation in a two-electrode setup. In the CV measurements, a reference electrode for alkaline solutions was used, which was calibrated with a Ag/AgCl/KCl (sat.) electrode. The potentials were converted to the RHE scale using the Nernst equation. In the two-electrode characterization, a platinum wire was utilized as a cathode, connected directly to the photoelectrode through an ammeter. In both PEC characterizations, the photoelectrodes were irradiated with a power density of 100 mW/cm^2 using a 300 W Xe arc lamp filtered with a UV spectroscopic mirror[25]. The number of absorbable photons by GaN (wavelength < 362 nm) in our light irradiation setup was 3.8×10^{16} cm^{-2} s^{-1}, which is about 11 times the number of absorbable photons in the AM 1.5G solar spectrum. The two-electrode characterizations were done in rounds of 10 h each, and during these characterizations, the amount of the gases generated on the electrodes was recorded and they were characterized later using gas chromatography. The faradaic efficiencies of the H_2 generation were calculated using the next equation

$$\eta_F = \frac{\eta_H P}{(1.23\ V)(\bar{J})} \tag{2}$$

where η_H is the H_2 ECE described by Eq. (1), P is the irradiation power density (100 mW/cm^2), $\bar{J}$ is the average current density of the photoelectrode and 1.23 V represent the difference in formal potentials of the hydrogen-evolution and oxygen-evolution half-reactions.

AFM profiles. The topographic profiles of the GaN electrodes after their PEC characterizations were measured with an Agilent 5500 Scanning Probe Microscope with a Bruker RTESPA-300 probe.

Conclusions

The PEC characterizations performed showed an improvement of the catalytic activity in a GaN photoelectrode when it is covered by Fe_2O_3 particles as cocatalyst. We found that the H_2 generation rate is about 5 times higher in a Fe_2O_3/GaN electrode compared with a bare GaN electrode. Besides, while the photocorrosion in the bare GaN electrode was macroscopically observed after just 2 h of PEC characterization, some minor photocorrosion damage was observed in the Fe_2O_3/GaN electrode only after 43 h.

In the study of the crystalline properties of the cocatalyst particles, we identified that they keep an epitaxial relationship with GaN, which follows the $Fe_2O_3\{0003\}||GaN\{0001\}$ and $Fe_2O_3[11\bar{2}0]||GaN[1\bar{1}00]$ symmetry constraints. When the Fe_2O_3 was deposited as a thin film, we observed a different epitaxial relationship, with the $Fe_2O_3\{11\bar{2}0\}||GaN\{0002\}$ and $Fe_2O_3[3\bar{3}00]||GaN[11\bar{2}0]$ symmetry constraints. However, the thin film cocatalyst did not show any improvement of the catalytic properties of GaN.

The incorporation of Fe_2O_3 onto the surface of a GaN photoelectrode improved its chemical endurance as well as its photocatalytic activity. Thus, Fe_2O_3 proved to be a suitable cocatalyst of GaN, which expands the technological applications possibilities of nitride-based semiconductors.

Data availability

All data generated or analysed during this study are included within the article (and its supplementary information) or are available from the corresponding author upon reasonable request.

Received: 3 March 2020; Accepted: 10 July 2020
Published online: 28 July 2020

References

1. Fujishima, A. & Honda, K. Electrochemical photolysis of water at a semiconductor electrode. *Nature* **238**, 37–38 (1972).
2. Brunner, D. *et al.* Optical constants of epitaxial AlGaN films and their temperature dependence. *J. Appl. Phys.* **82**, 5090–5096 (1997).
3. Chichibu, S. F. *et al.* Excitonic emission dynamics in homoepitaxial AlN films studied using polarized and spatio-time-resolved cathodoluminescence measurements. *Appl. Phys. Lett.* **103**, 142103 (2013).
4. Araki, T. *et al.* Radio frequency-molecular beam epitaxial growth of InN epitaxial films on (0001) sapphire and their properties. *J. Vac. Sci. Technol. B Microelectron. Nanom. Struct.* **22**, 2139–2143 (2004).
5. Vurgaftman, I. & Meyer, J. R. Band parameters for nitrogen-containing semiconductors. *J. Appl. Phys.* **94**, 3675–3696 (2003).
6. Fujii, K. *et al.* Band-edge energies and photoelectrochemical properties of n-type Al[sub x]Ga[sub 1–x]N and In[sub y]Ga[sub 1–y]N alloys. *J. Electrochem. Soc.* **154**, B175 (2007).
7. Moses, P. G. & Van De Walle, C. G. Band bowing and band alignment in InGaN alloys. *Appl. Phys. Lett.* **96**, 2–5 (2010).
8. Moses, P. G., Miao, M., Yan, Q. & Van De Walle, C. G. Hybrid functional investigations of band gaps and band alignments for AlN, GaN, InN, and InGaN. *J. Chem. Phys.* **134**, 084703 (2011).
9. Fujii, K., Karasawa, T. & Ohkawa, K. Hydrogen gas generation by splitting aqueous water using n-type GaN photoelectrode with anodic oxidation. *Jpn. J. Appl. Phys. Part 2 Lett.* **44**, 543–545 (2005).
10. Ono, M. *et al.* Photoelectrochemical reaction and H_2 generation at zero bias optimized by carrier concentration of n -type GaN. *J. Chem. Phys.* **126** (2007).
11. Hayashi, T., Deura, M. & Ohkawa, K. High stability and efficiency of GaN photocatalyst for hydrogen generation from water. *Jpn. J. Appl. Phys.* **51**, 50–52 (2012).
12. Ohkawa, K., Ohara, W., Uchida, D. & Deura, M. Highly stable GaN photocatalyst for producing H_2 gas from water. *Jpn. J. Appl. Phys.* **52**, 2–4 (2013).
13. Yotsuhashi, S. *et al.* Photo-induced CO_2 reduction with GaN electrode in aqueous system. *Appl. Phys. Express* **4**, 2–4 (2011).
14. Yotsuhashi, S. *et al.* Enhanced CO_2 reduction capability in an AlGaN/GaN photoelectrode. *Appl. Phys. Lett.* **100**, 2010–2013 (2012).
15. Hashiba, H., Yotsuhashi, S., Deguchi, M., Yamada, Y. & Ohkawa, K. Selectivity control of CO_2 reduction in an inorganic artificial photosynthesis system. *Appl. Phys. Express* **6**, 2–5 (2013).
16. Sekimoto, T. *et al.* Analysis of products from photoelectrochemical reduction of $^{13}CO_2$ by GaN-Si based tandem photoelectrode. *J. Phys. Chem. C* **120**, 13970–13975 (2016).
17. Grimaud, A. *et al.* Activating lattice oxygen redox reactions in metal oxides to catalyse oxygen evolution. *Nat. Chem.* **9**, 457–465 (2017).
18. Yoo, J. S., Rong, X., Liu, Y. & Kolpak, A. M. Role of lattice oxygen participation in understanding trends in the oxygen evolution reaction on perovskites. *ACS Catal.* **8**, 4628–4636 (2018).
19. Nørskov, J. K. *et al.* Origin of the overpotential for oxygen reduction at a fuel-cell cathode. *J. Phys. Chem. B* **108**, 17886–17892 (2004).
20. Koper, M. T. M. Theory of multiple proton–electron transfer reactions and its implications for electrocatalysis. *Chem. Sci.* **4**, 2710–2723 (2013).
21. Hou, Y. *et al.* Enhanced water splitting with silver decorated GaN photoelectrode. *J. Phys. D. Appl. Phys.* **49**, 265601 (2016).
22. Yoshida, M. *et al.* ATR-SEIRAS investigation of the fermi level of Pt cocatalyst on a GaN photocatalyst for hydrogen evolution under irradiation. *J. Am. Chem. Soc.* **131**, 13218–13219 (2009).
23. Maeda, K., Teramura, K., Saito, N., Inoue, Y. & Domen, K. Photocatalytic overall water splitting on Gallium nitride powder. *Bull. Chem. Soc. Jpn.* **80**, 1004–1010 (2007).
24. Alqahtani, M. *et al.* InGaN/GaN multiple quantum well photoanode modified with cobalt oxide for water oxidation. *ACS Appl. Energy Mater.* **1**, 6417–6424 (2018).
25. Velazquez-Rizo, M., Iida, D. & Ohkawa, K. Photoelectrochemical H 2 generation from water using a CoO x /GaN photoelectrode. *Jpn. J. Appl. Phys.* **58**, SCCC23 (2019).
26. Sivula, K., Le Formal, F. & Grätzel, M. Solar water splitting: progress using hematite (α-Fe_2O_3) photoelectrodes. *Chemsuschem* **4**, 432–449 (2011).
27. Tamirat, A. G., Rick, J., Dubale, A. A., Su, W. N. & Hwang, B. J. Using hematite for photoelectrochemical water splitting: a review of current progress and challenges. *Nanoscale Horizons* **1**, 243–267 (2016).
28. Tsyganok, A., Klotz, D., Malviya, K. D., Rothschild, A. & Grave, D. A. Different roles of Fe1-xNixOOH cocatalyst on hematite (α-Fe_2O_3) photoanodes with different dopants. *ACS Catal.* **8**, 2754–2759 (2018).
29. Hung, W. H., Chien, T. M. & Tseng, C. M. Enhanced photocatalytic water splitting by plasmonic TiO_2-Fe_2O_3 cocatalyst under visible light irradiation. *J. Phys. Chem. C* **118**, 12676–12681 (2014).

30. Xia, L. *et al.* High-performance $BiVO_4$ photoanodes cocatalyzed with an ultrathin α-Fe_2O_3 layer for photoelectrochemical application. *Appl. Catal. B Environ.* **204**, 127–133 (2017).
31. Yang, J., Li, D., Zhang, Z., Li, Q. & Wang, H. A study of the photocatalytic oxidation of formaldehyde on Pt/Fe_2O_3/TiO_2. *J. Photochem. Photobiol. A Chem.* **137**, 197–202 (2000).
32. Wei, Z., Wei, X., Wang, S. & He, D. Preparation and visible-light photocatalytic activity of α-Fe_2O_3/γ-Fe_2O_3 magnetic heterophase photocatalyst. *Mater. Lett.* **118**, 107–110 (2014).
33. Sealy, C. P., Castell, M. R. & Wilshaw, P. R. Mechanism for secondary electron dopant contrast in the SEM. *J. Electron Microsc. (Tokyo)* **49**, 311–321 (2000).
34. Akasaki, I., Amano, H., Kito, M. & Hiramatsu, K. Photoluminescence of Mg-doped p-type GaN and electroluminescence of GaN p-n junction LED. *J. Lumin.* **48–49**, 666–670 (1991).
35. Oshimura, Y. *et al.* AlGaN/GaN HFETs on Fe-doped GaN substrates. In *Physica Status Solidi* (*C*) *Current Topics in Solid State Physics* vol. 7 1974–1976 (2010).
36. Heikman, S., Keller, S., Denbaars, S. P. & Mishra, U. K. Growth of Fe doped semi-insulating GaN by metalorganic chemical vapor deposition. *Appl. Phys. Lett.* **81**, 439–441 (2002).
37. Mulmudi, H. K. *et al.* Controlled growth of hematite (α-Fe_2O_3) nanorod array on fluorine doped tin oxide: synthesis and photoelectrochemical properties. *Electrochem. Commun.* **13**, 951–954 (2011).
38. Van Aken, P. A., Liebscher, B. & Styrsa, V. J. Quantitative determination of iron oxidation states in minerals using Fe L2,3-edge electron energy-loss near-edge structure spectroscopy. *Phys. Chem. Miner.* **25**, 323–327 (1998).
39. Douglas, B. E. & Ho, S.-M. *Structure and Chemistry of Crystalline Solids. Structure and Chemistry of Crystalline Solids* (Springer, New York, 2006). https://doi.org/10.1007/0-387-36687-3.
40. Suturin, S. M. *et al.* Tunable polymorphism of epitaxial iron oxides in the four-in-one ferroic-on-GaN system with magnetically ordered α-, γ-, ϵ-Fe_2O_3, and Fe_3O_4 layers. *Phys. Rev. Mater.* **2**, 73403 (2018).
41. Chen, Z. *et al.* Accelerating materials development for photoelectrochemical hydrogen production: standards for methods, definitions, and reporting protocols. *J. Mater. Res.* **25**, 3–16 (2010).
42. Ito, K., Ikeda, S., Yoshida, M., Ohta, S. & Iida, T. On the reduction products of carbon dioxide at a p-type gallium phosphide photocathode in aqueous electrolytes. *Bull. Chem. Soc. Jpn.* **57**, 583–584 (1984).
43. Minsky, M. S., White, M. & Hu, E. L. Room-temperature photoenhanced wet etching of GaN. *Appl. Phys. Lett.* **68**, 1531–1533 (1996).
44. Youtsey, C., Adesida, I. & Bulman, G. Highly anisotropic photoenhanced wet etching of n-type GaN. *Appl. Phys. Lett.* **71**, 2151–2153 (1997).
45. Fujii, K. *et al.* Investigation of surface morphology of n-type GaN after photoelectrochemical reaction in various solutions for H_2 gas generation. In *Physica Status Solidi* (*C*) *Current Topics in Solid State Physics* vol. 4 2650–2653 (Wiley, 2007).
46. Zhang, X., Cao, C. & Bieberle-Hütter, A. Orientation sensitivity of oxygen evolution reaction on hematite. *J. Phys. Chem. C* **120**, 28694–28700 (2016).
47. Iwaki, Y. *et al.* Nitride photocatalyst to generate hydrogen gas from water. *Phys. Status Solidi Curr. Top. Solid State Phys.* **5**, 2349–2351 (2008).

Acknowledgements

This work was financially supported by the King Abdullah University of Science and Technology (KAUST) baseline funding BAS/1/1676-01-01 and start-up funding BAS/1/1676-01-08.

Author contributions

M.V.R., D.I. and K.O. jointly designed the experiments. M.V.R. wrote the first version of the manuscript and carried out the experiments and characterizations. D.I. and K.O. guided through the whole experimental process and substantially contributed to the revision of the manuscript.

Competing interests

The authors declare no competing interests.

Additional information

Supplementary information is available for this paper at https://doi.org/10.1038/s41598-020-69419-8.

Correspondence and requests for materials should be addressed to K.O.

Reprints and permissions information is available at www.nature.com/reprints.

Publisher's note Springer Nature remains neutral with regard to jurisdictional claims in published maps and institutional affiliations.